Modeling and control of LCL-filtered grid-tied inverters with wide inductance variation

Xie, Chuan; Li, Kai; Zhang, Gang; Zou, JianXiao; Guerrero, Josep M.

Published in:
Proceedings of 43rd Annual Conference of the IEEE Industrial Electronics Society, IECON 2017

DOI (link to publication from Publisher):
10.1109/IECON.2017.8216220

Publication date:
2017

Document Version
Early version, also known as pre-print

Modeling and Control of *LCL*-filtered Grid-Tied Inverters with Wide Inductance Variation

Chuan Xie, Kai Li, Gang Zhang and JianXiao Zou
School of Automation Engineering
UESTC, Chengdu, Sichuan 611731, China
Email: {c.xie, zhanggang jxzou}@uestc.edu.cn,
autolikai@gmail.com

Josep M. Guerrero
Department of Energy Technology
Aalborg University, Aalborg 9220, Denmark
Email: joz@et.aau.dk

***Abstract*—Because of the low power losses and moderate cost, the magnetic powder cores are popular in producing the filtering inductors for the high efficient and cost-effective power converters. However, the soft magnetic property of the powder cores leads to the wide variation of inductance along with the changing of the inductor current in one cycle of the grid, which challenges the system stability and power quality. In this paper, the current-dependent small-signal model of a three-phase *LCL*-filtered inverter is derived for designing the corresponding controller. Based on the developed small-signal model, a capacitor current feedback based active damping loop and a fractional order repetitive control based compound current control loop are designed to stabilize the system and enhance the control accuracy in steady-state, respectively. The controller design procedure is given in detail. Finally, all-digital simulation has been conducted on a 3.7 kVA inverter system to verify the theoretical expectations.**

Keywords—LCL filter; active damping; inductor nonlinearity; magnetic permeability; fracational order repetitive control.

I. INTRODUCTION

Driven by the economic and environmental issues, distributed power generation systems (DPGS) based on renewable sources, such as wind, photovoltaic, etc., are attracting more and more attentions[1], [2]. As an interface between DPGS and the power gird, the grid-connected inverter plays a vital role in converting the generated power into high quality ac power and injecting it into the grid. The major concerns of an inverter design include component selection, control scheme, electromagnetic interference, etc.

In order to reduce the harmonics of the inverter output current, output filters are often required. The *LCL*-type filter is increasingly adopted due to its better attenuation of the switching harmonics and much reduced inductance requirement. However, the *LCL*-type filter suffers from stability issue, various active damping methods have been studied to address this issue, such as converter side current feedback[3], grid side current feedback[4], capacitor current feedback[5] and voltage feedback[6], etc. The effect of sampling and PWM transport delays on the effectiveness of active damping methods has been investigated in [7], three distinct regions of *LCL* filter resonance have been identified. Compensating the delay in active damping loop can improve the system robustness, which can be achieved by shifting the capacitor current sampling instant towards the PWM reference update instant [8] or using the lead-lag compensator[9]. The optimal range of time delay and compensation method with single grid current feedback to improve the system performance has also been carefully studied [10]. The inductors of the *LCL* filter exhibit nonlinear and time-varying characteristic, which compromise the stability of the current controlled system, was explored in [11]. The repetitive control and resonant control have been used to improve the output current quality of the single *L*-filtered grid inverter under 25% inductance variation[11]. A single phase high power density inverter is designed in [12] by using the magnetic powder core based inductor with wide inductance variation and the corresponding division-summation digital control was proposed in [13]. Nevertheless, all existing discussions were limited to the simple *L* or *LC* filters. Its effect on the grid-tied inverters with *LCL* filters has not been discussed.

In this paper, a three-phase *LCL*-filtered grid-tied inverter system with more than 40% inductance variation is studied. Firstly, the current-dependent small-signal model of a three-phase *LCL*-filtered inverter is developed. Then, on the basis of the current-dependent model, a capacitor current feedback based active damping loop and a fractional order repetitive control based compound current control loop are designed. The rest of the paper is organized as follows: Section II will briefly introduce the system to be studied, the inductor parameter design and the mathematic model development. The system control strategy design procedure is given in detail in Section III. The waveforms are analyzed and discussed in Section IV. Finally, Section V concludes the paper.

II. MODELLING OF INVERTER WITH WIDE INDUCTANCE VARIATION

Fig. 1 shows the circuit topology of a *LCL*-filtered three-phase grid-connected inverter. L_1, L_2 and C_f denote the converter side inductor, grid side inductor and filter capacitor, respectively. C is the dc-side capacitor. R_1 and R_2 are the equivalent parasitic resistance of the inductors. The equivalent parasitic resistance of

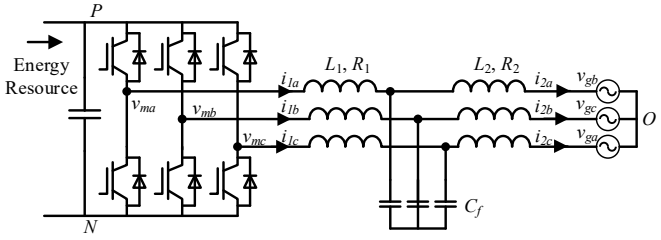

Fig. 1. Three-phase inverter connected to the grid through a *LCL*-filter.

capacitors are relatively small and, thus, are neglected here. v_{gk} ($k = a, b, c$) denotes the grid voltages, which are measured for the purpose of synchronizing the control. i_{1k} and i_{2k} ($k = a, b, c$) are the inverter-side and grid-side current, respectively. The nominal value of main circuit parameters are listed in Table I.

A. Design of Inductors with Magnetic Powder Cores

Sendust core as one kind of magnetic power cores is well known for the moderate cost and lower losses and relatively high saturation level, which make it popular in designing high efficiency and high power density converters. The sendust core based inductor is chosen as an example for studying. Fig. 2 shows the curves of permeability for sendust cores with different initial permeability. It can been seen that the core with higher initial permeability has larger drop under the same magnetizing force. Obviously, if the small inductance tolerance is required, the core with small initial permeability should be used. However, it will lead to big core size and weight, and more turns. If a larger initial permeability core is selected, the same inductance can be achieved with relative smaller size and weight and less turns.

The nominal value of the inductor used in this study is set to 2 mH at 8 A. Two inductors are designed by using two sendust cores with different initial permeability. The parameters of the magnetic powder core and designed inductors are illustrated in Table II. It can been seen that the winding factors of the two inductors are 7.4% and 15%, respectively, which indicates that the inductors are achievable. It also can be seen that both the size and weight of the type one inductor's core are two times bigger than that of type two inductor. The inductor turns can be reduced by applying higher initial permeability core. The calculated inductance of the two designed inductors corresponding to inductor currents 0 to 10A are depicted in Fig. 3. Although the type two inductor has smaller size and weight, the inductance

TABLE I. NOMINAL VALUE OF MAIN CIRCUIT PARAMETERS

Symbol	Quantity	Value
$L_{1,nom}$	Converter side inductor	2mH
$R_{1,nom}$	parasitic resistance of L_1	0.2Ω
$L_{2,nom}$	Grid side inductor	2mH
$R_{2,nom}$	parasitic resistance of L_1	0.2Ω
$C_{f,om}$	Capacitor of LCL-filter	10 uF

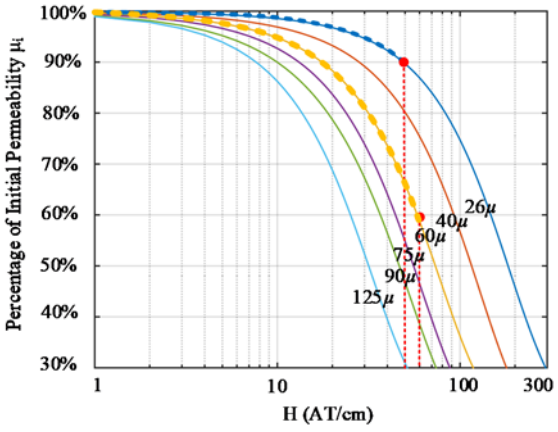

Fig. 2. Curves of permeability versus DC bias for different sendust cores[14].

TABLE II. THE PARAMETERS OF THE MAGNETIC POWDER CORE AND DESIGNED INDUCTORS

		Type one	Type two
Core parameters	Initial Permeability	26μ	60μ
	Outer Diameter	134.0 mm	62.91 mm
	Inner Diameter	77.19 mm	31.69 mm
	Height	26.8 mm	25.91 mm
	Weight	1.2 kg	0.34 kg
	Inductance factor	68 nH/T^2	189 nH/T^2
Inductor parameters	Turns	181	128
	Wire area	1.84 mm^2	1.84 mm^2
	Winding factor	7.4%	15%

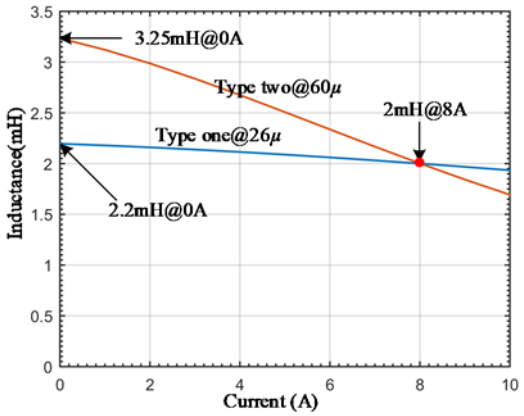

Fig. 3. Calculated inductance of the two designed inductors versus the current variations.

varying widely when inductor current varies from 0 to rated value. This may challenge the design of control strategy.

B. Modeling of the Inverter with Wide Inductance Variation

Since the inductance is dependent on inductor current value, it is expressed as a function of current as follow:

$$L(i) = f(i). \tag{1}$$

Neglecting the parasitic resistor of inductor, the capacitor is assumed to be constant while the inductor value is time variant, the averaged state-space model for *LCL*−filter in the *abc*-frame can be obtained as following by applying the state-space averaging technique [15].

$$\dot{X} = AX + BU \tag{2}$$

where X, U, A, B are listed at the bottom of next page.

Assuming that the inductance are constant at any steady-state operation point (i_{1a}, i_{1b}, i_{1c}, i_{2a}, i_{2b}, i_{2c}, v_{ca}, v_{cb}, v_{cc}, v_{ma}, v_{mb}, v_{mc},v_{ga}, v_{gb}, v_{gc}), where the small signal model can be obtained by applying the small-signal linearization technique to (2). Then applying the *Laplace* transform to small-signal state-space model, the s-domain transfer function can be achieved.

G_{m2}(s) is the transfer function from inverter output v_m(s) to the grid current i_2(s), which can be derived as follows:

$$G_{m2}(s) = \frac{i_2(s)}{v_m(s)} = \frac{1}{L_1(i_1)L_2(i_2)C_f s} \cdot \frac{1}{s^2 + \omega_r^2}. \tag{3}$$

where ω_r is the resonance angular frequency, which can be expressed as

$$\omega_r = \sqrt{\frac{L_1(i_1)+L_2(i_2)}{L_1(i_1)L_2(i_2)C_f}}\,.$$

$G_{mc}(s)$ is the transfer function from inverter output $v_m(s)$ to the capacitor current $i_c(s)$ in d-axis as shown

$$G_{mc}(s) = \frac{i_c(s)}{v_m(s)} = \frac{1}{L_1(i_1)} \cdot \frac{s}{s^2+\omega_r^2}\,. \tag{4}$$

Since the control algorithms are implemented in discrete time domain. Eq. (3) and (4) are transformed into z-domain via zero order hold (ZOH) transformation as follows.

$$\begin{aligned} G_{m2}(z) &= Z\{(1-e^{-T_s s})\frac{G_{m2}(s)}{s}\} \\ &= \frac{\omega_r T_s[z^2-2\cos(\omega_r T_s)z+1]-\sin(\omega_r T_s)(z-1)^2}{\omega_r[L_1(i_1)+L_2(i_2)](z-1)[z^2-2\cos(\omega_r T_s)z+1]} \end{aligned} \tag{5}$$

$$\begin{aligned} G_{mc}(z) &= Z\{(1-e^{-T_s s})\frac{G_{mc}(s)}{s}\} \\ &= \frac{\sin(\omega_r T_s)}{\omega_r L_1(i_1)} \cdot \frac{z-1}{z^2-2\cos(\omega_r T_s)z+1} \end{aligned} \tag{6}$$

where T_s represents the sampling period.

III. Control Strategy Design

The control of the system is composed of a capacitor-current feedback active damping loop and a fractional order repetitive controller based compound current control loop.

A. Active Damping Compensator

Fig. 4 shows the block diagram of the capacitor-current feedback active damping loop with a lead-lag compensator, where z^{-1} element represents the computation delay, $L(z)$ represents lead-lag compensator. The open loop transfer function of the active damping loop $T_{mc}(z)$ can expressed as follow:

$$T_{mc}(z) = K_{ad} z^{-1} G_{mc}(z) L(z)\,. \tag{7}$$

where K_{ad} represent the active damping loop gain. The lead-lag compensator $L(z)$ can be expressed as

$$L(z) = \frac{z-1}{z-0.5}\,. \tag{8}$$

According to (7), two arrays of root loci of the active damping loop with inductance variation are drawn in Fig. 5. It can been seen that the root loci of the active damping loop without phase compensation almost always outside the unit circle, thus it's difficult to stabilize the system. By providing the lead-lag compensator to the active damping loop, the root loci moves towards inside of the unit circle, the stability can be improved. It also can be seen that the root loci are more inside

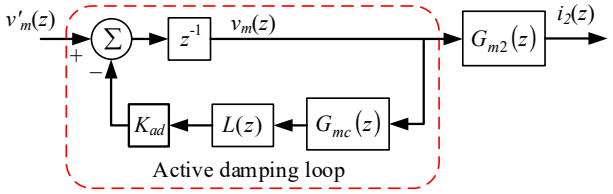

Fig. 4. Block diagram of capacitor-current feedback active damping loop with lead-lag compensator.

$$X = [i_{1a}, i_{1b}, i_{1c}, i_{2a}, i_{2b}, i_{2c}, v_{ca}, v_{cb}, v_{cc}]^T,\ U = [v_{ma}, v_{mb}, v_{mc}, v_{ga}, v_{gb}, v_{gc}]^T,$$

$$A = \begin{bmatrix} 0 & 0 & 0 & 0 & 0 & 0 & \frac{-1}{L_1(i_{1a})} & 0 & 0 \\ 0 & 0 & 0 & 0 & 0 & 0 & 0 & \frac{-1}{L_1(i_{1b})} & 0 \\ 0 & 0 & 0 & 0 & 0 & 0 & 0 & 0 & \frac{-1}{L_1(i_{1c})} \\ 0 & 0 & 0 & 0 & 0 & 0 & \frac{-1}{L_2(i_{2a})} & 0 & 0 \\ 0 & 0 & 0 & 0 & 0 & 0 & 0 & \frac{-1}{L_2(i_{2b})} & 0 \\ 0 & 0 & 0 & 0 & 0 & 0 & 0 & 0 & \frac{-1}{L_2(i_{2c})} \\ \frac{1}{C_f} & 0 & 0 & \frac{-1}{C_f} & 0 & 0 & 0 & 0 & 0 \\ 0 & \frac{1}{C_f} & 0 & 0 & \frac{-1}{C_f} & 0 & 0 & 0 & 0 \\ 0 & 0 & \frac{1}{C_f} & 0 & 0 & \frac{-1}{C_f} & 0 & 0 & 0 \end{bmatrix},$$

$$B = \begin{bmatrix} \frac{1}{L_1(i_{1a})} & 0 & 0 & 0 & 0 & 0 \\ 0 & \frac{1}{L_1(i_{1b})} & 0 & 0 & 0 & 0 \\ 0 & 0 & \frac{1}{L_1(i_{1c})} & 0 & 0 & 0 \\ 0 & 0 & 0 & \frac{-1}{L_2(i_{2a})} & 0 & 0 \\ 0 & 0 & 0 & 0 & \frac{-1}{L_2(i_{2b})} & 0 \\ 0 & 0 & 0 & 0 & 0 & \frac{-1}{L_2(i_{2c})} \\ 0 & 0 & 0 & 0 & 0 & 0 \\ 0 & 0 & 0 & 0 & 0 & 0 \\ 0 & 0 & 0 & 0 & 0 & 0 \end{bmatrix}.$$

of the unit circle when the current is small and the inductance is larger, on contrast, the root loci is more approaching to the unit circle when current is large and the inductance becomes small. For better damped, the active damping loop gain K_{ad} is set to 5.

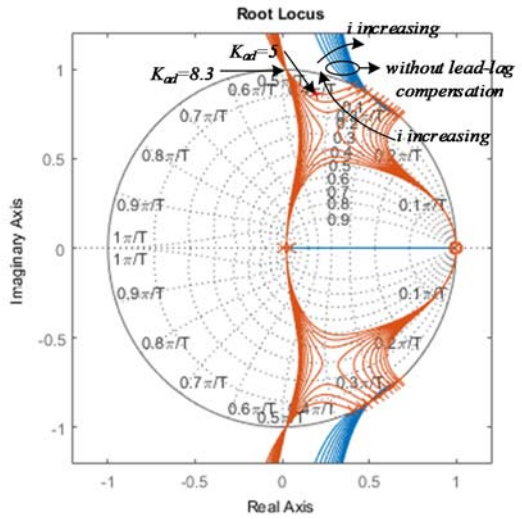

Fig. 5. Root loci of active damping loop with/withtou lead-lag compensation.

B. Inner PI Control Loop

Fig. 6 shows the block diagram of the inner PI control loop in z-domain. The open loop and closed loop transfer functions can be derived as:

$$T_{m2}(z)=\frac{PI(z)z^{-1}G_{m2}(z)}{1+K_{ad}z^{-1}G_{mc}(z)L(z)}=\frac{PI(z)z^{-1}G_{m2}(z)}{1+T_{mc}(z)}, \quad (9)$$

$$T_2(z)=\frac{T_{m2}(z)}{1+T_{m2}(z)}. \quad (10)$$

According to (9), an array of root loci for inner PI control loop considering inductance variation are drawn in Fig. 7. It can be seen that the root loci are always inside the unit circle for $0 < K_p < 11$. Finally, the proportional gain K_p is set to 5 to achieve smooth magnitude characteristics of closed-loop, which is depicted in Fig. 8. It also can been seen from Fig. 8 that the harmonic control capability of the inner PI control loop is very limited due to the large phase lag in the Bode plot of the closed-loop. To improve the steady-state control precision for harmonics, the fractional order repetitive controller is added.

C. External Fractional Order Repetitive Control Loop

Fig. 9 shows the block diagram of plug-in fractional order repetitive control loop. The transfer function of the FORC can be expressed as [16]:

$$G_{fr}(z)=\frac{u_r(z)}{e(z)}=\frac{z^{-N_i}Q(z)H(z)}{1-z^{-N_i}Q(z)H(z)}S(z). \quad (11)$$

where N_i is the integral part of the ratio N, $N=f_s/f$ with f_s being the sampling frequency and f being the fundamental frequency of the grid. $S(z)$ is a compensator consists of a pure leading element, and $Q(z) = a_1z + a_0 + a_1z^{-1}$ with $2a_1 + a_0 = 1$ is a low-pass filter (LPF) to improve the robustness of the system[16].

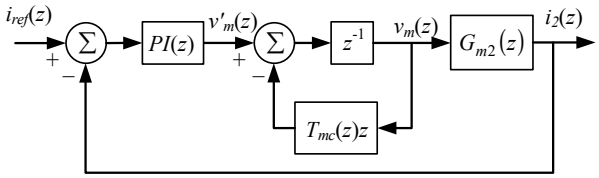

Fig. 6. Block diagram of inner PI control loop in z-domain.

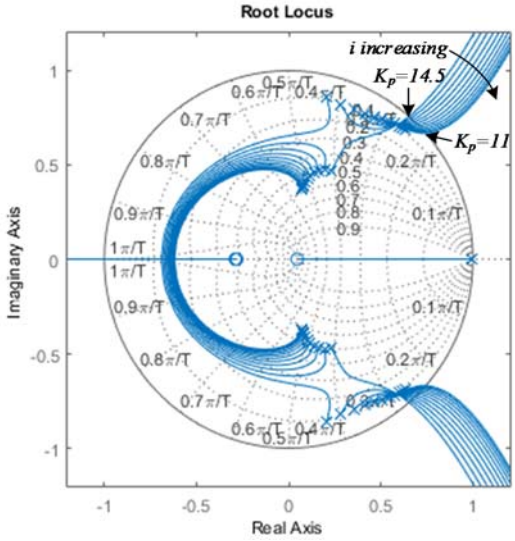

Fig. 7. Root loci of inner PI control loop.

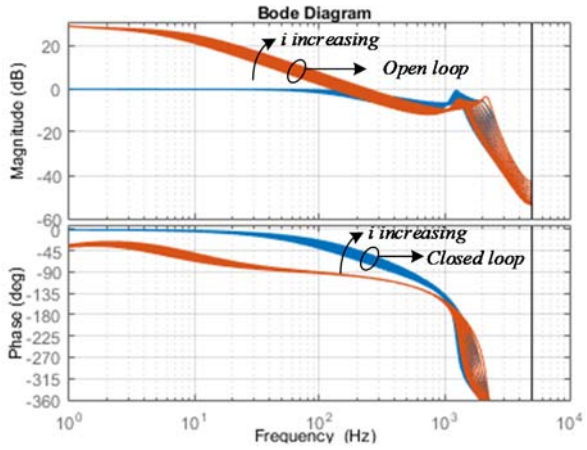

Fig. 8. Bode plots of open/closed transfer function for inner PI control loop.

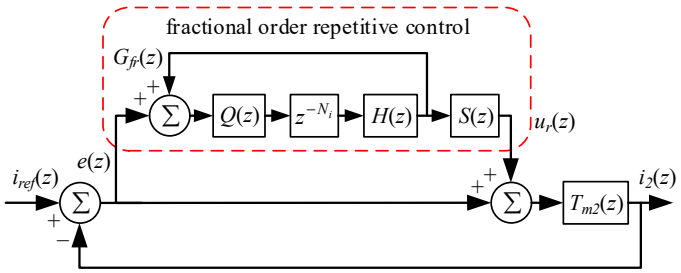

Fig. 9. Block diagram of plug-in fractional order repetitive control loop.

$H(z)$ is a Lagrange interpolation polynomial FIR filter, which can be expressed as follow:

$$H(z)=\sum_{k=0}^{n}h(k)z^{-k} \text{ with } h(k)=\prod_{i=0,i\neq k}^{n}\frac{F-i}{k-i}. \quad (12)$$

where n is the order of FIR filter, F is the fractional part of the ratio N.

According to Fig. 9, the error transfer function of the overall system can be derived as

$$\frac{e(z)}{I_{ref}(z)}=\frac{1-z^{-N_i}H(z)}{1-z^{-N_i}H(z)Q(z)[1-S(z)T_2(z)]}\cdot\frac{1}{1+T_{m2}(z)} \quad (13)$$

The closed-loop FORC system is asymptotically stable if the following two conditions are held [16].

1) The roots of $1+T_{m2}(z)=0$ are inside the unit circle.

2) The following inequality equation holds.

$$\left|H(z)Q(z)[1-S(z)T_2(z)]\right|<1. \quad (14)$$

Assuming $T(z)=Q(z)[1-S(z)T_2(z)]$, the magnitude of $H(z)$ is always no larger than 1, thus, a more conservative stability condition can be derived as:

$$\left|T(z)\right|<1. \quad (15)$$

Fig. 10 shows the phase-frequency characteristic curves of $T_2(z)$,$1/S(z)$ and $S(z)T_2(z)$. It can be seen that the phase lag of delay z^{-5} agrees well with that of $T_2(z)$, thus, $S(z)$ is set to z^5 to compensate the delay of $T_2(z)$.

Fig. 11 illustrates an array of *Nyquist* curves of $T(z)$ with wide inductance variations. The Nyquist curves are all inside the unit circle, thus the system stability condition are always held.

IV. Simulation Results

To validate feasibility of the designed control strategy for the three-phase *LCL*-filtered grid-tied inverter shown in Fig. 1, simulation has been carried out in MATLAB/Simulink emulating as close as possible the discrete behavior of the DSP and the analog hardware components of a real setup.

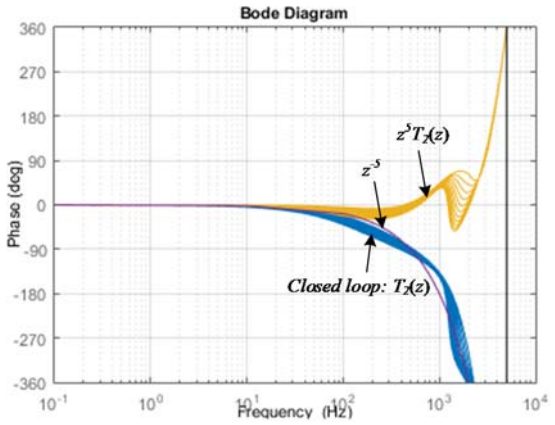

Fig. 10. Phase-frequency characteristic curves of $T_2(z)$,$1/S(z)$ and $S(z)T_2(z)$.

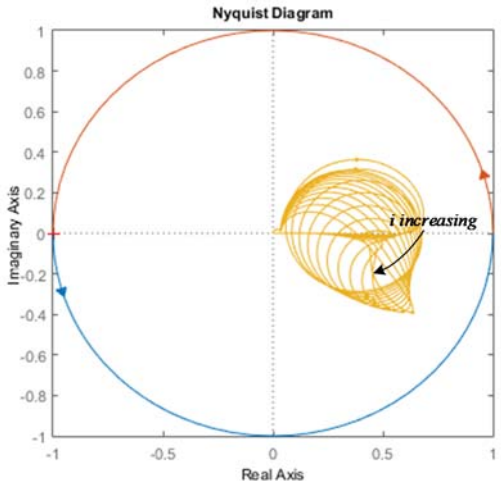

Fig. 11. Nyquist curves of $T(z)$ with wide inductance variations.

A. Steady State Performance

The inverter has been tested under the distorted grid with total harmonic distortion (THD) equals to 4.6%. As shown in Fig. 12(a), with only PI control the inverter output current is distorted with THD equals to 12.5%. When FORC has been activated, the THD of the inverter output current is reduced to 2.1%, as shown in Fig. 12(b) and (c).

The variation of inductance for both grid side and current side inductors are also shown in Fig. 12(a) and (b). It can been seen that the inductance varies between 2 mH and 3.2 mH along with the changing of inductor current.

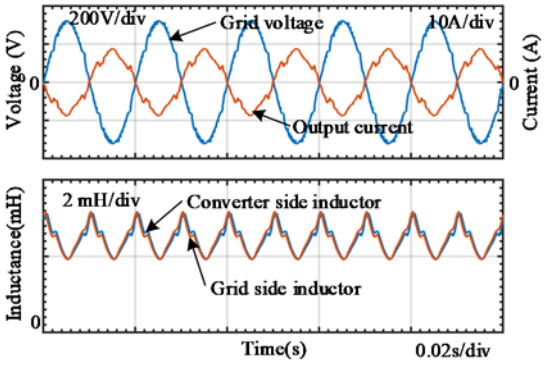

(a)

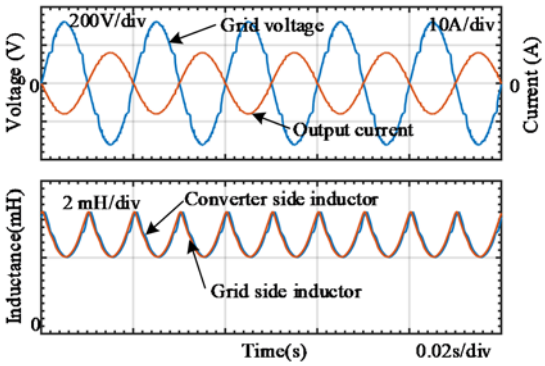

(b)

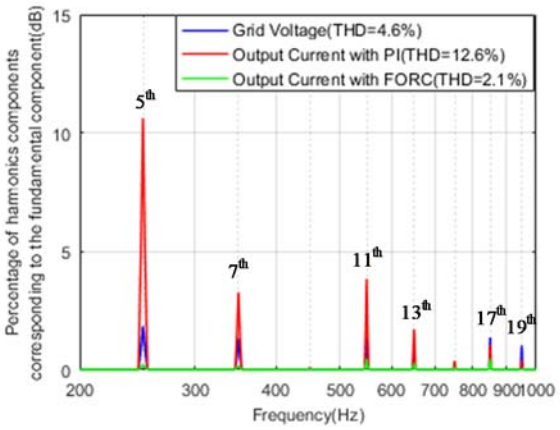

(c)

Fig. 12. Steady-state waveforms and spectra of inverter output current with (a) Only PI control and (b) fractional order repetitive control.

B. Dynamic Response Performance

The dynamic response performance of the inverter also has been tested by changing of the current reference in d-axis (corresponding to the active power current component). The test result is shown in Fig. 13, where from up to bottom are reference and inverter output currents in d-axis and q-axis, respectively. It can been seen that the dynamic response time is about 0.05s, which is mainly caused by the FORC.

V. CONCLUSITONS

Applying the high permeability magnetic power core can obtain more compact, lighter and cost-effective inductors for inverters. However, it will result in wide inductance variation. Aiming to stably operate the *LCL*-filtered grid-tied inverter with wide inductance variation, the control strategy has been carefully designed.

Firstly, the current-dependent small-signal model of the *LCL*-filtered three-phase inverter with inductance variation is derived. To stabilize the *LCL*-filter, a capacitor current feedback based active damping method is adopted and a lead-lag compensator is added to enhance stability margin. Meanwhile, a fractional order repetitive control has also been used to improve the harmonic control capability.

Simulation results validate the feasibility and effectiveness of proposed control strategy. Laboratory experimental verification will be conducted in the future.

ACKNOWLEDGEMENT

This work was supported in part by the Sichuan Science and Technology Support Program (No. 2016GZ0027 and No. 2017GZ0051) and in part by Fundamental Research Funds for the Central Universities (No. ZYGX2014J069 and No. ZYGX2015J075).

REFERENCES

[1] J. M. Guerrero, P. C. Loh, T.-L. Lee, and M. Chandorkar, "Advanced Control Architectures for Intelligent Microgrids—Part II: Power Quality, Energy Storage, and AC/DC Microgrids," *IEEE Trans. Ind. Electron.*, vol. 60, no. 4, pp. 1263–1270, Apr. 2013.

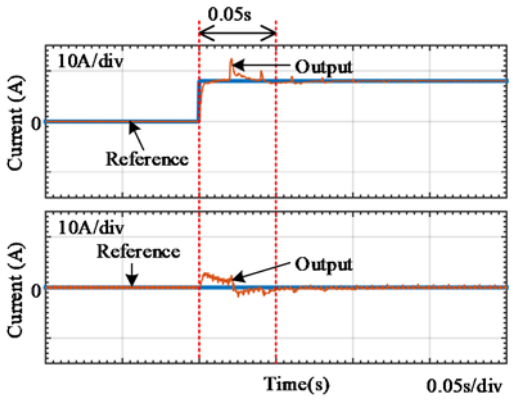

Fig. 13. Dynamic waveforms of inverter output current during the step up of the current reference.

[2] D. Liu, F. Deng, and Z. Chen, "Five-Level Active-Neutral-Point-Clamped DC/DC Converter for Medium-Voltage DC Grids," *IEEE Trans. Power Electron.*, vol. 32, no. 5, pp. 3402–3412, May 2017.

[3] M. Liserre, A. Dell'Aquila, and F. Blaabjerg, "Stability improvements of an LCL-filter based three-phase active rectifier," in *Power Electronics Specialists Conference, 2002. pesc 02. 2002 IEEE 33rd Annual*, 2002, vol. 3, pp. 1195–1201.

[4] J. Yin, S. Duan, and B. Liu, "Stability Analysis of Grid-Connected Inverter With LCL Filter Adopting a Digital Single-Loop Controller With Inherent Damping Characteristic," *IEEE Trans. Ind. Inform.*, vol. 9, no. 2, pp. 1104–1112, May 2013.

[5] E. Twining and D. G. Holmes, "Grid current regulation of a three-phase voltage source inverter with an LCL input filter," *IEEE Trans. Power Electron.*, vol. 18, no. 3, pp. 888–895, May 2003.

[6] V. Blasko and V. Kaura, "A novel control to actively damp resonance in input LC filter of a three-phase voltage source converter," *Ind. Appl. IEEE Trans. On*, vol. 33, no. 2, pp. 542–550, 1997.

[7] S. G. Parker, B. P. McGrath, and D. G. Holmes, "Regions of active damping control for LCL filters," in *Energy Conversion Congress and Exposition (ECCE), 2012 IEEE*, 2012, pp. 53–60.

[8] D. Pan, X. Ruan, C. Bao, W. Li, and X. Wang, "Capacitor-Current-Feedback Active Damping With Reduced Computation Delay for Improving Robustness of LCL-Type Grid-Connected Inverter," *IEEE Trans. Power Electron.*, vol. 29, no. 7, pp. 3414–3427, Jul. 2014.

[9] C. Chen, J. Xiong, Z. Wan, J. Lei, and K. Zhang, "Time Delay Compensation Method Based on Area Equivalence for Active Damping of LCL-Type Converter," *IEEE Trans. Power Electron.*, vol. PP, no. 99, pp. 1–1, 2016.

[10] X. Wang, F. Blaabjerg, and P. Loh, "Grid-Current-Feedback Active Damping for LCL Resonance in Grid-Connected Voltage Source Converters," *IEEE Trans. Power Electron.*, vol. PP, no. 99, pp. 1–1, 2015.

[11] R. A. Mastromauro, M. Liserre, and A. D. Aquila, "Study of the Effects of Inductor Nonlinear Behavior on the Performance of Current Controllers for Single-Phase PV Grid Converters," *IEEE Trans. Ind. Electron.*, vol. 55, no. 5, pp. 2043–2052, May 2008.

[12] T.-F. Wu, H.-S. Nien, C.-L. Shen, and T.-M. Chen, "A Single-Phase Inverter System for PV Power Injection and Active Power Filtering With Nonlinear Inductor Consideration," *IEEE Trans. Ind. Appl.*, vol. 41, no. 4, pp. 1075–1083, Jul. 2005.

[13] T.-F. Wu, C.-H. Chang, L.-C. Lin, G.-R. Yu, and Y.-R. Chang, "A D-Σ Sigma Digital Control for Three-Phase Inverter to Achieve Active and Reactive Power Injection," *IEEE Trans. Ind. Electron.*, vol. 61, no. 8, pp. 3879–3890, Aug. 2014.

[14] Magnetics, "2015 Magnetics Powder Core Catalog." [Online]. Available: www.mag-inc.com.cn.

[15] E. Twining, D. G. Holmes, and others, "Modeling grid-connected voltage source inverter operation," *Proc APEC'01*, pp. 501–506, 2001.

[16] Z.-X. Zou, K. Zhou, Z. Wang, and M. Cheng, "Frequency-Adaptive Fractional-Order Repetitive Control of Shunt Active Power Filters," *IEEE Trans. Ind. Electron.*, vol. 62, no. 3, pp. 1659–1668, Mar. 2015.